J Solid State Electrochem (2018) 22:1495–1506
https://doi.org/10.1007/s10008-017-3802-1

ORIGINAL PAPER

Niobium: a promising Pd co-electrocatalyst for ethanol electrooxidation reactions

F. Moura Souza[1] · L. S. Parreira[2] · P. Hammer[3] · B. L. Batista[1] · M. C. Santos[1]

Received: 5 July 2017 / Revised: 3 October 2017 / Accepted: 9 October 2017 / Published online: 18 October 2017

Abstract This work reports the sol–gel synthesis and characterization of Pd_xNb_y/C binary electrocatalysts applied to ethanol electrooxidation reactions (EORs). Catalysts were prepared using different Pd/Nb mass ratios (1:0; 1:1; 1:3; 3:1; 0:1) and were supported on Vulcan XC-72 carbon (20 wt%). The materials were characterized by transmission electron microscopy, energy-dispersive X-ray spectroscopy, X-ray diffraction, inductively coupled plasma mass spectrometry, and X-ray photoelectron spectroscopy. The EOR catalytic activity was studied by cyclic voltammetry (CV) and chronoamperometry (CA). The results showed that the EOR current density peak using Pd_1Nb_1/C (45.5 mA mg^{-1}) was 2.86 times higher than that of commercial Pd/C (15.9 mA mg^{-1}). This catalyst also showed a less positive EOR onset potential and 2.35 times higher current density than Pd/C did in CA. The Pd_1Nb_1/C (− 0.54 V) showed onset potential more negative than Pd/C (− 0.50 V) for CO-stripping analysis. Additionally, the addition of Nb in the Pd/C reduces CO_{ads} poisoning of the electrocatalyst. The results suggest that Nb decreases the poisoning effect of CO on the Pd surface due to the bifunctional mechanism in which Nb supplies oxygenated species for CO oxidation at poisoned Pd active sites. No evidence of Pd/Nb alloy formation has been found. The maximization of the bifunctional effect occurs in Pd_1Nb_1/C.

Keywords Alkaline direct ethanol fuel cells · Ethanol electrooxidation reaction · Palladium nanoparticles · Niobium nanoparticles

Introduction

A sustainable energy transformation technology is one that can replace a dependence on fossil fuels and reduce the emission of pollutants into the Earth's atmosphere. Among the most promising directions of these sustainable technologies is the direct ethanol fuel cell (DEFC), which converts chemical energy at high efficiency and emits a low level of pollutants if the chemical fuel is from a renewable source [1, 2].

However, the electrooxidation reaction (EOR) that produces carbon dioxide (CO_2) from ethanol has been a challenge due to the difficulty of C-C bond cleavage and the formation of intermediates that block the active sites of the electrocatalyst [3, 4]. Therefore, in order to obtain a higher yield of the complete oxidation of ethanol to CO_2, it is necessary to study new electrocatalysts that are more active and selective.

Previous studies have shown that palladium (Pd) is approximately four times better than Pt as catalyst under alkaline conditions, especially in the case of ethanol oxidation [5, 6]. In the last 5 years, the use of Pd as electrocatalyst in alkaline DEFCs has shown promising results and is an interesting alternative for studies [7, 8]. As the amount of Pd on Earth is higher than that of Pt, its exploration and trade occur with lower costs [9]. The economic advantages of using other metals (Ni, Pd and Sn) than the Pt or gold (Au) as

Electronic supplementary material The online version of this article (https://doi.org/10.1007/s10008-017-3802-1) contains supplementary material, which is available to authorized users.

✉ M. C. Santos
mauro.santos@ufabc.edu.br

[1] LEMN—Centro de Ciências Naturais e Humanas (CCNH), Universidade Federal do ABC (UFABC), CEP 09.210-170, Rua Santa Adélia 166, Bairro Bangu, Santo Andre, SP, Brazil

[2] Instituto de Química, Universidade de São Paulo, Av. Prof. Lineu Prestes, 748, Sao Paulo, SP 05508-000, Brazil

[3] Instituto de Química de Araraquara, Departamento de Físico-Química, Universidade Estadual Paulista (UNESP), Araraquara, SP 14800-900, Brazil

electrocatalysts are evident when comparing the price of a gram of each metal [10].

To facilitate the oxidation of intermediates, such as CO, acetate and acetaldehyde, which decrease the performance of the fuel cell, auxiliary metals are added to the pure effective metal, in this case Pd, to form binary and ternary alloys [11, 12].

Materials containing niobium (Nb) also received special attention for their use in heterogeneous catalysis. Many studies have showed that the use of small concentrations of Nb increased catalytic activity, selectivity and chemical stability of traditional catalysts. There has been an increasing interest in the application of these materials, especially Nb oxides, as active phases or supports. The wide variation of the Nb–O bond of structures and their combination with other oxides result in unique properties that allow these alloys to be used as catalysts for many reactions [13].

The adsorption of carbon monoxide (CO), a by-product formed after the oxidation of small organic molecules (such ethanol), decreases the number of active sites of the electrocatalyst. It has been claimed that the use of the auxiliary metals decreases this adsorption of CO at the Pd active sites [10, 14].

Numerous metals have been used as auxiliary electrocatalysts for some mechanisms in the oxidation reactions that favour the activity of the electrocatalyst. The most accepted mechanisms in these processes are the bifunctional mechanism and the electronic effect.

Recent researchers have obtained good results with Pd nanoelectrocatalysts. Electrocatalysts such as PdAu [15] and PdPt [16] with different nanoparticle shapes have been recently developed and shown an increasing catalytic activity of Pd for EOR. Geraldes et al. [9] studied a series of carbon-supported Pd and Sn binary alloyed catalysts for ethanol electrooxidation in alkaline media. Among several Pd and Sn catalysts, $Pd_{86}Sn_{14}$/C catalysts enhanced current densities in cyclic voltammetry and chronoamperometry measurements compared to commercial Pd/C (Johnson Matthey Company).

Sun et al. [17] have compared the electrochemical activity of Pd–Ru and Pt–Ru and showed that Pd–Ru in alkaline media is approximately 4-fold better than Pt–Ru for EORs. Yi et al. [18] studied porous Pd–Ru nanoparticles that were supported on titanium prepared by a hydrothermal method. Regarding current density and onset potentials, they reported that $Pd_{87}Ru_{13}$ showed the best catalytic activity towards EORs in alkaline media. They also suggested that the "bifunctional mechanism" and the large surface area of $Pd_{87}Ru_{13}$ are the real reasons for the improvement of the electrochemical activities [19].

Efforts in combining Pd with a second metal that can be either noble, e.g., Ru, Au, and Rh, or non-noble metals such as Fe, Co, Ni, Cu, and Mo have been shown to improve catalytic activity [10, 20–22]. However, there are very few reports of Pd–Nb binary electrocatalysts. As far as we know, there have been no research articles on the electrochemical activity of these electrocatalysts for EORs. In addition, there is no work that is similar to this study in the literature, specifically, using a sol–gel method to produce Pd and Nb.

In the current work, we investigated the surface, structure, composition and EOR activity of Pd_xNb_y/C electrocatalysts in alkaline media. The nanoparticles (NPs) were prepared using a sol–gel method and then supported on Vulcan XC-72 carbon. The NPs were characterized, and the electrocatalytic activity was investigated using cyclic voltammetry (CV) and chronoamperometry (CA) techniques.

Materials and methods

Preparation of the electrocatalysts

The electrocatalysts were prepared by adapting the sol–gel method [23]. For this, Pd–acetylacetonate (99% Sigma-Aldrich®, product by USA) and $NbCl_5$ (99% Sigma-Aldrich® product by Germany) were mixed with 6 mL of isopropyl alcohol (Synth®) and 2 mL of acetic acid (Synth®). Next, the Vulcan XC-72 carbon was added. The sol–gel solution was homogenized by magnetic stirring and heated for 60 min to dryness. The samples were submitted to heat treatment in the muffle under an N_2 atmosphere. The samples were heated at 5 °C min^{-1} in three steps: 110 °C for 15 min, 400 °C for 60 min and then cooled at a rate of 10 °C min^{-1} until the sample reaches room temperature.

Electrochemical measurements

Electrochemical cell

The materials were electrochemically characterized, and their catalytic activity was evaluated by CV and CA by using an Autolab 302N potentiostat. The electrolyte was KOH (1.0 mol L^{-1}) with or without the presence of ethanol (1.0 mol L^{-1}). A conventional electrochemical cell with a three electrode configuration was used and included a 1-cm^2 platinum electrode as the counter electrode, Hg/Hg_2Cl_2 (SCE) as the reference electrode and the working electrode was the studied electrocatalyst supported on a glassy carbon electrode.

The three electrodes were arranged in a 40-mL cell that contained the N_2-degassed (to reduce O_2 intervention) electrolyte solution. For the analysis in the presence of ethanol, 2.34 mL of ethanol (99.5% Dinâmica®, Brazil) was introduced into the working solution to obtain a concentration of 1.0 mol L^{-1} for both CV and CA tests. All the experiments were carried out at room temperature.

Preparation of the working electrode

For the preparation of the electrocatalyst, we used approximately 8 mg of the metal/carbon mixture. Next, we added

1 mL of high purity deionized water (resistivity 18.2 MΩ cm, Millipore water purification system, Millipore, Bedford, MA, USA) and sonicated this mixture for 40 min. After homogenization, 20 μL of Nafion® solution (5% *m*/*v*) was added, and the mixture was sonicated for 30 min, generating a black and homogeneous dispersion. Finally, 10 μL of this dispersion was added to the working electrode (glassy carbon) and dried using a tungsten lamp.

CO-stripping analysis

CO stripping experiment was performed in a 1-mol L^{-1} KOH solution under the potential range from 0.8 to 0.1 V, and the scan rate was set at 10 mV s^{-1}. Before the experiment, ultrapure N_2 (99.99%) was purged through 1 mol L^{-1} KOH solution during 30 min to remove CO monolayer previously adsorbed. After that, the catalyst modified electrode was immersed into the KOH solution and CO was bubbled for 10 min to allow the adequate adsorption of CO (99.9%) onto the surface of the catalyst while the potential of working electrode was kept at − 0.1 V vs. SCE. Hence, the CO excess in the solution was removed by bubbling N_2 (99.99%) during 20 min. The experiments were performed at room temperature.

Experimental characterization

XRD analysis

All electrocatalysts were physically characterized using X-ray diffraction (XRD). The equipment was a Rigaku-MiniFlex X-ray diffractometer with a Cu Kα radiation source operating continuously (2° min^{-1}) from 20° to 90° (2θ) to determine the crystalline phases and to estimate the mean crystallite sizes.

Elemental composition by ICP-MS analysis

The elemental composition of the electrocatalyst was determined using an inductively coupled plasma mass spectrometer (ICP-MS, Agilent 7900, Hachioji, Japan) with high-purity argon (99.9999%, White Martins, Brazil). All reagents were of analytical grade. Nitric acid and HCl were purified by using a Teflon subboiling distiller (DST-100, Savillex, USA). High-purity deionized water (resistivity 18.2 MΩ cm) was generated with a Milli-Q water purification system (Millipore, Bedford, MA, USA). The Pd and Nb extraction was carried out using a closed vessel system. Approximately, 30 mg of electrocatalyst was placed into 100 mL tubes that contained 3 mL of HNO_3 + 1 mL of HCl, and the tubes were then closed. Then, the tubes stood for 24 h at 25 °C. After this step, they were heated at 200 °C for 2 h in a graphite-covered digester block (EasyDigest, Analab, France). Finally, the volume was increased to 50 mL, and the elemental composition was determined by ICP-MS. The ICP-MS conditions are described in Table 1. The calibration curve ranged from 1 to 50 μg L^{-1} for Pd and Nb and resulted in R^2 = 0.9999.

EDS

EDS analyses were performed using an EDS chemical microanalysis module that was coupled to a JSM-6010LA Compact Sweep Electron Microscope (JEOL). EDS analyses were obtained using the map mode with at least three measurements, and each part of the sample that was mapped was averaged.

TEM

To observe the morphology and to measure the particle sizes, transmission electron microscopy (TEM) analyses were performed using a high-resolution JEOL JEM-2100 electron transmission microscope operating at 200 kV. Samples for TEM studies were prepared by placing nanodispersion droplets on a carbon-coated copper grid, and the solvent (water) was evaporated at room temperature. The average particle size was determined using the ImageJ software package (v.1.50i; product of Wayne Rasband, National Institutes of Health, USA), and more than 300 different electrocatalyst particles were analysed.

X-ray photoelectron spectroscopy

The XPS analysis was carried out at a pressure of less than 10^{-7} Pa using a commercial spectrometer (UNI-SPECS UHV). The Al Kα line was used ($h\nu$ = 1486.6 eV), and the analyser pass energy was set to 10 eV. The inelastic background of Pd 3d, Nb 3d and C 1s high-resolution core-level spectra was subtracted using Shirley's method [24]. The binding energy scale of the spectra was corrected using the C 1s CC-sp^2 peak at 284.5 eV. The spectra were fitted without placing constraints using multiple Voigt profiles with the CasaXPS software (v.2.3.13; product of CasaXPS Software

Table 1 Operational conditions for ICP-MS

Monitored isotopes	^{105}Pd, ^{93}Nb
Limit of detection	0.004 μg L^{-1} Pd, 1.93 μg L^{-1} Nb
Internal standard	^{89}Y (25 μg L^{-1})
Radio frequency power	1550 W
Argon flow rate	15 L min^{-1}
Sample nebulizer pump	0.3 rps
Nebulizer gas flow rate	1.03 L min^{-1}
Sample depth	8 mm
Nebulizer	Mira Mist (Teflon)
Nebulizer chamber	Scott (double pass)
Interface	Nickel cones
Sampling cone	1 mm
Skimmer	0.9 mm

Table 2 Pd and Nb concentrations (mass ratios) obtained by using ICP-MS or EDS

Electrocatalyst	Pd nominal (%)	Pd ICP-MS (%)	Pd EDS (%)	Nb nominal (%)	Nb ICP-MS (%)	Nb EDS (%)
Pd/C	20.00	26.50 ± 2.64	26.62 ± 3.02	n.d.	n.d.	n.d.
Pd_1Nb_1/C	10.00	8.81 ± 0.56	10.74 ± 1.80	10.00	13.45 ± 3.58	9.15 ± 1.62
Pd_3Nb_1/C	15.00	13.72 ± 0.68	14.08 ± 0.63	5.00	4.55 ± 0.67	4.26 ± 0.89
Pd_1Nb_3/C	5.00	4.29 ± 0.11	4.35 ± 0.48	15.00	13.57 ± 1.87	15.28 ± 1.25

n.d. not determined

Ltd., USA). The full width at half maximum (FWHM) varied between 1.0 and 2.0 eV, and the accuracy of the peak positions were determined within ± 0.1 eV.

Results and discussion

Physical–chemical characterization

The mass ratios of Pd that were obtained by EDS and ICP-MS for Pd_xNb_y/C sol–gel electrocatalysts are summarized in Table 2. The results suggest that high percentages of Pd and Nb ions were converted to metal and chemically anchored to the carbon support (Vulcan XC-72). ICP-MS and EDS techniques, which use different physical properties for to accomplish sample quantification, showed similar Pd mass ratios in the electrocatalysts.

Results of SEM/EDS electrocatalyst mapping are shown in Supplementary Figs. S1 and S2, which are available in the supplemental electronic material. They indicate that the electrocatalysts are heterogeneous samples, as expected, and that the Pd and Nb atoms are well dispersed in all samples and completely cover Vulcan XC-72 carbon.

The X-ray diffractograms that are displayed in Fig. 1a show a broad peak that is centred at approximately $2\theta = 25°$ (Bragg angle) and was attributed to reflection plane (002) of the hexagonal structure of the Vulcan XC-72 carbon support. Figure 1a shows that there is a mixture of Pd and PdO_2 crystalline phases with predominant formation of a PdO_2 (002) tetragonal crystalline system that is evidenced by the peak at $2\theta = 33.84°$. Figure 1b, which is an approximation of the diffractogram of the sample in Fig. 2a, shows that there is also a mixture of Nb and Nb_2O_5. The predominant crystalline phase was Nb_2O_5 (111) of the monoclinic crystalline system at $2\theta = 23.82°$. In Fig. 1a, b, Pd_xNb_y/C electrocatalysts showed that Pd (fcc) peaks were not shifted to the peaks that represent Pd electrocatalysts; therefore, no Pd–Nb alloys were formed.

The predominance of crystalline phases in the form of oxides suggests that the bifunctional mechanism is the main factor affecting the increased Pd_1Nb_1/C electrochemical activity for the EOR. In the bifunctional mechanism, the effective metal operates as the adsorption and dehydrogenation site of ethanol. The auxiliary metal promotes the oxidation of CO to CO_2 by using the oxygenated chemical species that is attached to it; in that way, the auxiliary metal reduces catalytic poisoning [18, 25]. This effect depends on having oxygenated species near the oxidation site of Pd to favour the oxidation of the CO intermediate to CO_2 [26].

Table 3 shows the summary of the peaks, chemical formula, crystalline systems, Miller indices and Crystallography Open Database (COD) IDs obtained by XRD of Pd_xNb_y/C electrocatalysts.

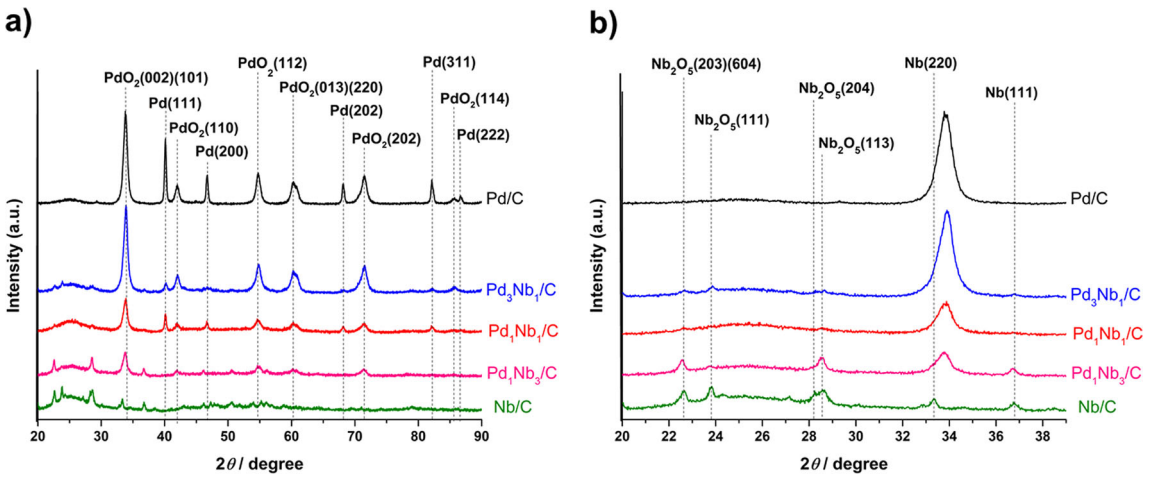

Fig. 1 **a** X-ray diffraction patterns of the Pd_xNb_y/C electrocatalysts in the range of $2\theta = 20°–90°$. **b** X-ray diffraction patterns of the Pd_xNb_y/C electrocatalysts in the range of $2\theta = 20°–40°$

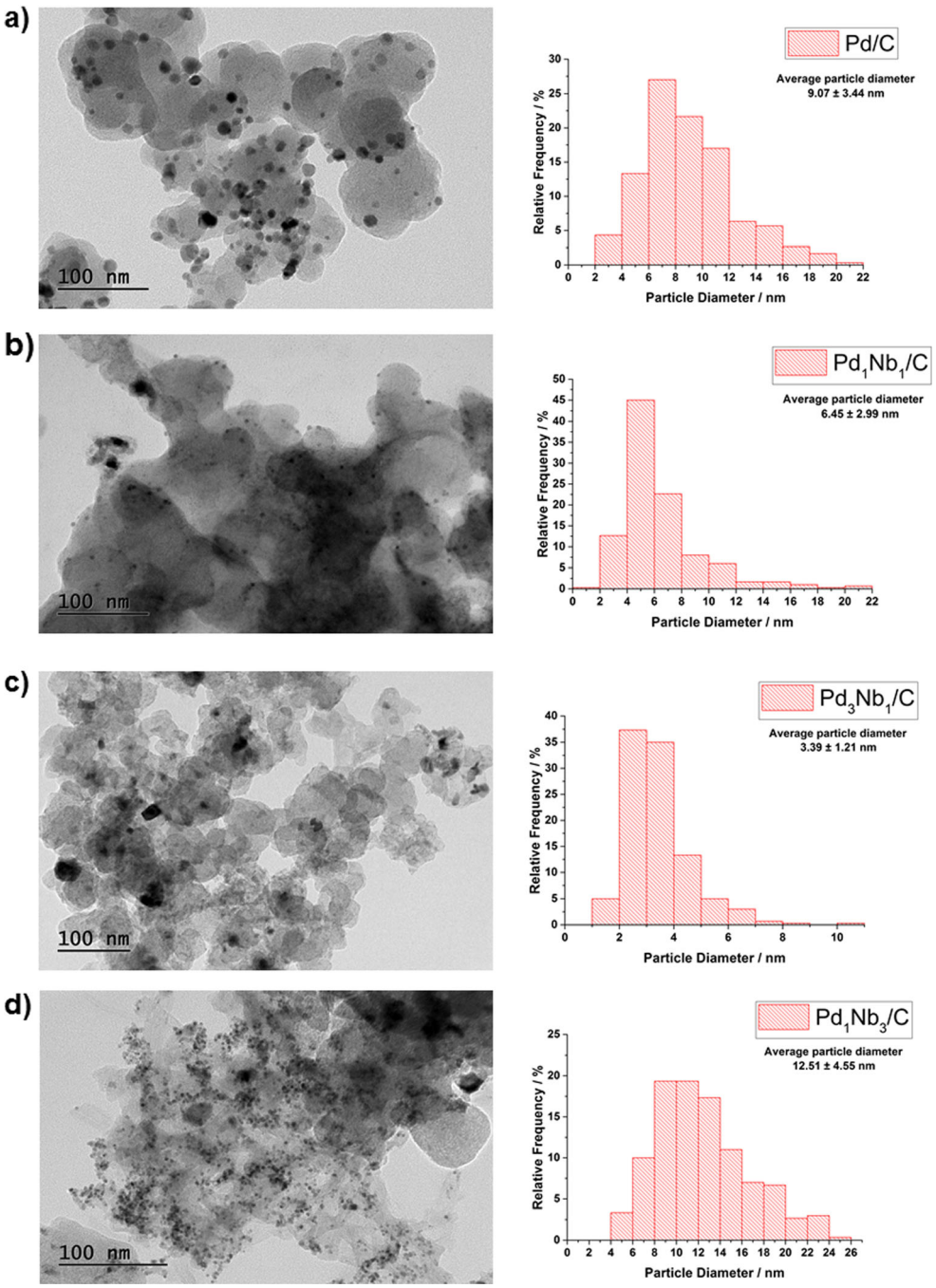

Fig. 2 TEM micrographs and particle size distribution histograms of **a** Pd/C, **b** Pd_1Nb_1/C, **c** Pd_3Nb_1/C and **d** Pd_1Nb_3/C electrocatalysts

The average sizes of the crystallite particles can be estimated using the Debye–Scherrer formula [27].

$$B_{2\theta} = \frac{0.94\lambda}{L\cos\theta} \quad (1)$$

in which $B_{2\theta}$ is the full width at half maximum, λ is the wavelength of the incident radiation, L is the particle diameter (crystallite size) and θ is the diffraction angle. The average crystallite size of the Pd_xNb_y/C electrocatalyst is calculated from the full widths at half maximum (FWHM) of the peaks (002), (111), (110), (200), (013), (202), (311), (114) and (222) of Pd or PdO_2 because it best represents all samples [28]. Thus, this approach considers the different sizes in each crystalline phase that are present in the sample. The final mean is the sum of the different calculated average crystallite sizes of each observed peak divided by the number of summed peaks. The results of the average crystallite size for Pd/C, Pd_1Nb_1/C, Pd_3Nb_1/C and Pd_1Nb_3/C electrocatalysts were 4.05 ± 1.64, 4.15 ± 1.10, 4.60 ± 1.34 and 4.73 ± 1.00 nm, respectively. This order suggests that the presence of Nb slightly increases the mean crystallite size of the nanoparticles.

Table 3 Identification of crystalline phases, Miller and crystal system by XRD analyses

This work		COD (Crystallography Open Database)			
Peak index	2θ	Formula	Crystal system	*hkl*	COD ID
1	22.64	Nb_2O_5	Monoclinic	(203)(604)	1534156
2	23.82			111	
3	28.24			204	
4	28.62			113	
5	33.34	Nb	fcc	220	1534903
6	33.84	PdO	Tetragonal	002	1011112
7	36.76	Nb	fcc	111	1534903
8	40.12	Pd	fcc	111	1011106
9	42.00	PdO	Tetragonal	110	1011112
10	46.70	Pd	fcc	200	1011106
11	54.74	PdO	Tetragonal	112	1011112
12	60.20			013	
13	60.78			200	
14	68.14	Pd	fcc	202	1011106
15	70.74	PdO	Tetragonal	004	1011112
16	71.50			202	
17	82.14	Pd	fcc	311	1011106
18	85.74	PdO	Tetragonal	114	1011112
19	86.66	Pd	fcc	222	1011106

The lattice parameters and the Pd–Pd mean interatomic distances were calculated from interplanar distance equation for a cubic crystalline system.

$$d_{hkl} = \frac{a^2}{h^2 + k^2 + l^2} \quad (2)$$

where d_{hkl} is the interplanar distance; h, k and l are the Miller indices; and a is the lattice parameter. The existing Pd fcc peak at $2\theta = 40.12°$, with Miller indices (111), was used to calculate the lattice parameter. The results in Table 4 indicate that there was no significant difference in the Pd lattice parameter with the addition of Nb. Thus, this result corroborates the previous ones that suggested the non-formation of metallic alloys of Pd and Nb.

Figure 2 shows typical images from the TEM study and graphs of the nanoparticle size distribution of the electrocatalysts. The Pd_xNb_y/C electrocatalyst showed a good distribution of nanoparticles on the carbon support, with an average particle diameter from 3 to 12 nm. The Pd nanoparticles in the Pd/C electrocatalyst showed a spherical shape and small numbers of hexagonal formations. The electrocatalysts that contain Nb did not present a pattern of formations.

The order of increasing mean nanoparticle size is Pd_3Nb_1/C < Pd_1Nb_1 < Pd/C < Pd_1Nb_3/C. Comparison with XRD average crystallite sizes showed that there were non-significant differences between the techniques. However, the results corroborate that the Pd_1Nb_3/C electrocatalyst is the sample with the largest diameter nanoparticles because of the presence of larger crystallites and nanoparticles from agglomerations. Pd_1Nb_1/C has the second smallest average crystallite and mean nanoparticle sizes. In addition, the average diameter of nanoparticles is between 4 and 6 nm; these NPs have better stability against agglomerations and better electrochemical activity per surface area [29].

Table 4 Interplanar distance and network parameter derived from XRD results

Electrocatalyst	2θ	d_{hkl} (nm)	a (nm)
Pd/C	40.20	0.2246	0.3889
Pd_1Nb_1/C	40.40	0.2245	0.3888
Pd_3Nb_1/C	40.18	0.2242	0.3884

Figure 3 presents HRTEM images. We can observe the crystallographic lattices of the electrocatalysts that exhibit the details of the interplanar distances between the layers of atoms in the crystalline structure of the metal nanoparticles, which were calculated from the micrographs.

The Pd/C micrograph shows a crystal lattice with interplanar spacing at 0.2306 nm, which is the interplanar spacing for Pd (fcc) according to peak index 8 in Table 3. The Pd_1Nb_1/C and Pd_1Nb_3/C micrographs show that the interplanar crystal lattices are 0.2145 and 0.2270 nm, respectively, which are characteristic of PdO_2 (tetragonal) according to peak index 9 (Table 3).

In the image of the electrocatalyst Pd_3Nb_1/C, it was possible to observe different crystallographic lattices: Nb_2O_5 (monoclinic), PdO_2 (tetragonal) and Pd (fcc), with the COD IDs 1534156, 1011112 and 1011106, respectively, that confirm the presence of different crystallographic systems that were previously observed in XRD spectra and mentioned above (Fig. 1; Table 3).

Electrochemical activity studies

The cyclic voltammetry (CV) of Pd_xNb_y/C electrocatalysts was first investigated in the 1 M KOH aqueous solution, and the results are shown in Fig. 4. The Pd_xNb_y/C electrode exhibits a typical feature of Pd electrodes in alkaline solution, in agreement with previous reports [30, 31]. All the Pd_xNb_y/C electrocatalysts appear to have similar columbic features as the Pd/C, such as formation (regions + 0.1 V to + 0.2 V) and reduction (regions − 0.2 to − 0.4 V) of PdOH and adsorption (region − 0.7 to − 0.8 V) and desorption (region − 0.6 V in the cathodic scans) of hydrogen. Moreover, in the anodic scans, all Pd_xNb_y/C electrocatalysts show a negative shift of peak potentials compared to those of Pd/C. The distinct anodic

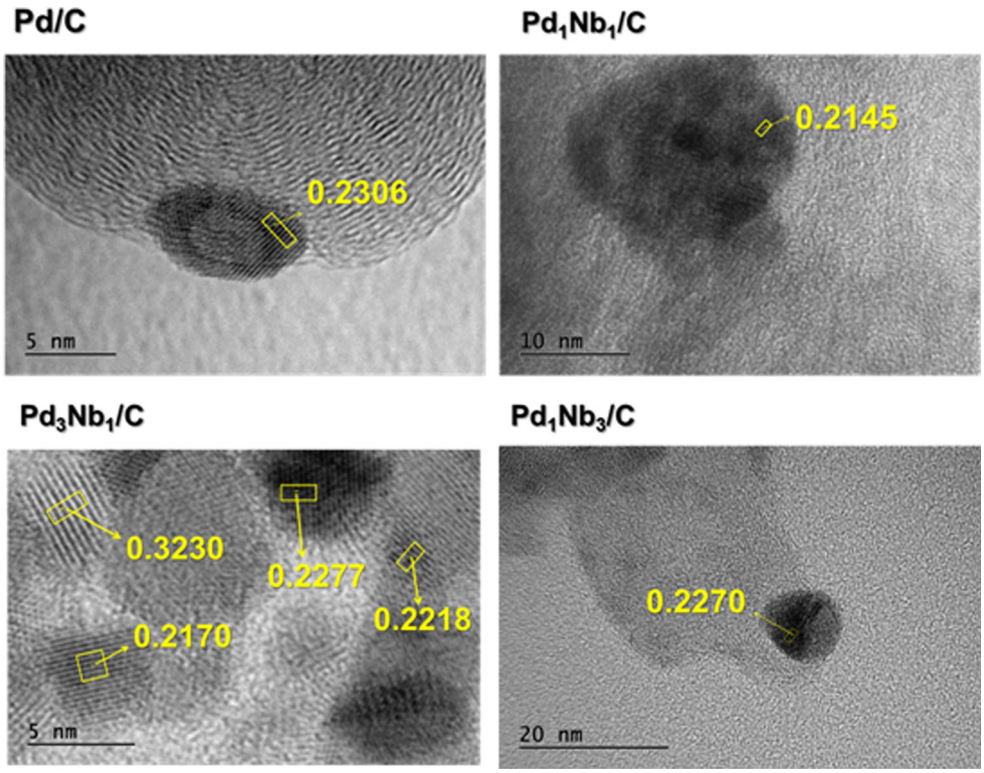

Fig. 3 HRTEM micrographs in detail, showing the crystal lattices of the Pd_xNb_yC electrocatalysts

(oxidation) behaviour on Pd–Nb/C and Pd/C electrocatalysts indicates that the electronic structure on the surface of Pd/C has changed after the insertion of Nb into the electrocatalysts.

In order to discuss both ECSA and the operation of bifunctional mechanism, CO stripping experiments were performed. CO poisoning is one of the main challenges for advancing DEFC technology [32]. In Fig. 5, we can identify that the electrocatalyst Pd_1Nb_1/C has the lowest onset potential (− 0.54 V) for CO oxidation, more negative than those of Pd/C (− 0.50 V), Pd_3Nb_1/C (− 0.38 V) and Pd_1Nb_3/C (− 0.35 V).

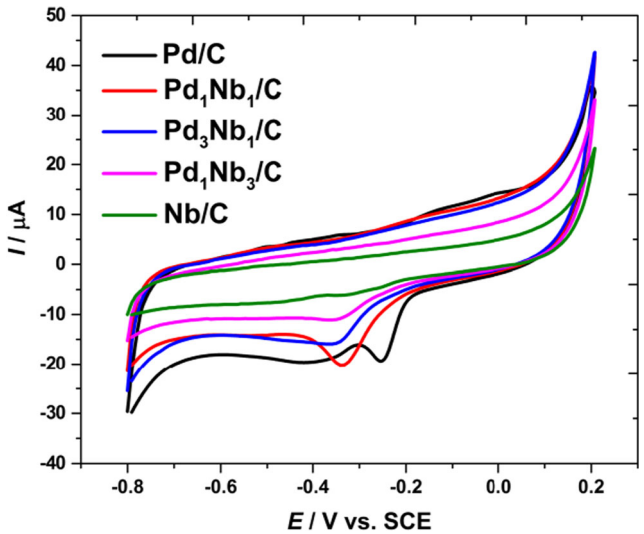

Fig. 4 Cyclic voltammograms of Pd_xNb_y/C electrocatalysts in 1.0 mol L^{-1} KOH at 25 °C, measured in a potential range from − 0.80 to + 0.20 V vs. SCE at a scan rate of 10 mV s^{-1}

It has been widely accepted that the CO stripping follows by the reaction between the formed OH_{ads} and CO_{ads} ($CO_{ads} + OH_{ads} \rightarrow CO_2 + H_2O$), where possibly Pd–$CO_{ads}$ and Nb–OH_{ads} react on the active sites [33–35].

The electrochemically active surface areas (ECSA) of the electrocatalysts were estimated by electrochemical oxidation of a pre-adsorbed saturated CO adlayer (CO_{ad} stripping, Fig. 5). The corresponding ECSA of the electrocatalysts were obtained from the equation [36]:

$$ESCA = \frac{Q}{G \times 420} \quad (3)$$

where Q is the charge of CO desorption–electrooxidation in micro-coulomb (μC), G represents the total amount of Pd (μg) on the electrode and 420 is the charge required to oxidize one monolayer of CO adsorbed at the catalyst in micro-coulomb per square centimetre. The increasing order of ECSA by CO-stripping is Pd_3Nb_1/C < Pd/C < Pd_1Nb_1/C < Pd_1Nb_3/C displaying Table 5.

Zhang et al. [37] reported an electrocatalyst Pd/Cu_3P/RGO with 40 m^2 g^{-1} of ECSA supported on reduced graphene oxide that has a high cost. For this reason, we were able to obtain 38 m^2 g^{-1} of ECSA on Pd_1Nb_1/C electrocatalyst, with a very low-cost Vulcan XC72 support. Although Pd_1Nb_3/C

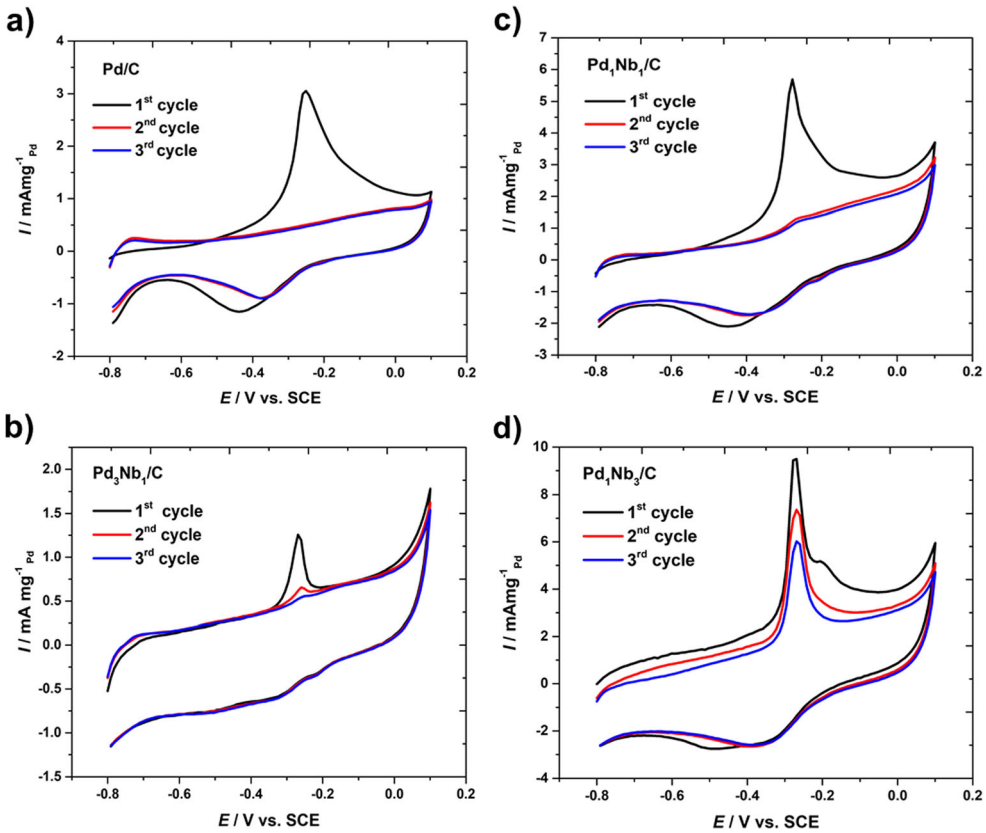

Fig. 5 CO stripping curves of **a** Pd/C, **b** Pd_3Nb_1/C, **c** Pd_1Nb_1/C and **d** Pd_1Nb_3/C electrocatalysts, in 1 mol L^{-1} KOH at a scan rate of 10 mV s^{-1}, at room temperature

showed higher current for CO-stripping, it remained CO poisoned in the second cycle and remains still in the third cycle after CO-stripping, as shown in Fig. 5d, this occurs probably due to adsorption strength on Pd sites for the case. This difficulty for CO desorption indicates that Pd_1Nb_3/C is less promising for EOR because of the ability to CO oxidize desorption correlates with catalytic activity in organic fuel oxidation. These results are suggested to be explained by the low amount of Pd (for Pd_1Nb_3/C) compared to the amount for those different electrocatalysts. Possibly, the form of CO adsorption on the surface of Pd was modified (strongly bounded CO adsorption forms maybe operating like bridge and or 3-fold). We have no direct experimental evidence for this, although the literature indicates that this is probably what happens [38–40]. Besides, both CO stripping (see Fig. 5d) and chronoamperometry experiments (see Fig. 7) hardly prove that CO poisoning and/or strongly bounded intermediates are in a highest amount for Pd_1Nb_3/C electrocatalysts, since these are necessary more cycles to CO desorption and the current in the chronoamperometry results for ethanol oxidation is the lowest. We suggest that Nb has a notable effect on improving CO-anti-poisoning activity of Pd-electrocatalyst mainly for Pd_1Nb_1/C electrocatalysts.

The voltammetric responses for ethanol oxidation using Pd/C, Pd_1Nb_1/C (50:50), Pd_3Nb_1/C (75:25), Pd_1Nb_3/C (25:75) and Nb/C electrocatalysts are shown in Fig. 6.

Table 5 ECSA results from CV of Pd_xNb_y/C electrocatalysts

Electrocatalyst	ECSA (m^2 g^{-1} Pd)
Pd/C	13
Pd_1Nb_1/C	29
Pd_3Nb_1/C	10
Pd_1Nb_3/C	47

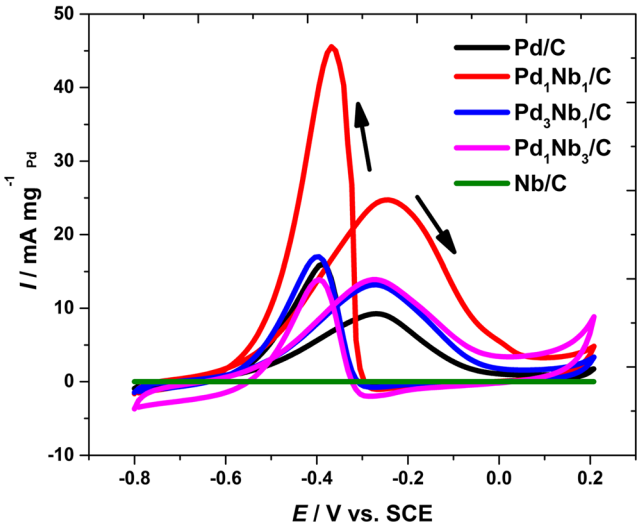

Fig. 6 Cyclic voltammograms of Pd_xNb_y/C electrocatalysts using 1.0 mol L^{-1} ethanol and 1.0 mol L^{-1} KOH, measured over a potential range from − 0.80 to + 0.20 V vs. SCE at a sweep rate of 10 mV s^{-1}

The cyclic voltammogram that was obtained from ethanol electrooxidation on the Pd_1Nb_1/C electrocatalyst showed the lowest onset potential: − 0.74 V vs. SCE. Although the centre of the ethanol oxidation peak is − 0.4 V vs. SCE in Fig. 6 for all electrocatalysts, the E_{onset} has different values which are more negative, as shown in Table 6. For example, in solution under study, zero RHE corresponds to ~ − 1.04 V SCE, so Pd_1Nb_1/C has E_{onset} − 0.74 V vs. SCE when converted to RHE is ~ − 0.30 V. As a fuel cell, cathode typically operates at ~0.85 V RHE. Thus, DEFC applications ($\Delta E_{cell} = E_c - E_a = 0.85 - (-0.30) \sim 1.15$ V). This result indicates that in fuel cell applications, this electrocatalyst will generate a great potential variation, which can be useful for electrical work.

The onset potential of the other Pd_xNb_y/C electrocatalysts is shown in Table 6. The Nb/C electrocatalyst did not exhibit any electrochemical activity for the oxidation of ethanol, as shown in Fig. 6. Therefore, metallic Nb or Nb oxide does not contribute individually to the ethanol electrooxidation reaction.

The electrocatalyst Pd_1Nb_1/C showed the best electrochemical activity for the oxidation of ethanol, with the highest peak current density in the CV, as shown in Fig. 6 and Table 6. The peak current density was 2.86 times higher than that of the Pd/C electrocatalyst. Jing-Jing et al. [12] reported PtPd NF-RGO/GCE with a current density of about 52 mA mg^{-1}. Although it is a higher electrochemical activity for EOR, the support used was of much higher cost than ours (Vulcan XC72). Considering the CV in Fig. 6, we can see that the peak current density is higher in the reverse potential scan than in the forward potential scan. Then, after the formation of intermediate species that are adsorbed on the Pd layer in the outward potential sweep that prevents the adsorption of new ethanol molecules, the reverse potential scan should have a lower current density peak. However, this expectation is not the case. This result suggests that the presence of Nb and Nb_2O_5 has facilitated the oxidation of intermediates due to the bifunctional effect [34]. Consequently, the sites are free again for the electrooxidation of ethanol.

Figure 7 shows the chronoamperometry results that were obtained at room temperature for 1800 s of ethanol electrooxidation reaction with the Pd_xNb_y/C electrocatalysts.

Table 6 Overview of electrochemical results CA and CV

Electrocatalyst	E_{onset} (V)	Peak current density (mA mg^{-1} Pd)	Current density at CA (mA mg^{-1} Pd)
Pd/C	− 0.72	15.9	0.72
Pd_1Nb_1/C	− 0.74	45.5	1.06
Pd_3Nb_1/C	− 0.69	16.9	0.53
Pd_1Nb_3/C	− 0.63	14.0	0.36

The prepared electrocatalysts were tested for 1800 s to evaluate their activity, stability and tolerance to poisoning by intermediate species. During the experiments, the current density reaches a stable condition, and the electrocatalyst stability can be evaluated. The peaks that occur in the first few seconds are due to charging of the electric double layer and the instability of the system under the conditions in which the experiment was performed. After this short interval, the system stabilized. For all electrocatalysts, the measurement showed a slow decrease in the current values for the electrocatalysts that were studied during the experiments. However, this decrease is slower for Pd_1Nb_1/C samples, as shown in Fig. 7. As before, the Nb/C electrocatalyst did not exhibit any electrochemical activity for the oxidation of ethanol.

From the graphs, it was observed that the electrocatalyst Pd_1Nb_1/C exhibited a less pronounced drop in the density current value than the other electrocatalysts. It was also observed that the electrocatalyst Pd_1Nb_1/C was the most active among all the evaluated samples. Its current density was 1.47 times higher than that of Pd/C, as shown in Table 6.

That is, it produced more energy in the same operating time. These results suggest that at the investigated electrode potential, the addition of Nb contributes to the activity and stability of Pd-based electrocatalysts and to the ethanol electrooxidation reaction, yielding electrocatalysts that are more efficient and more tolerant to poisoning. This fact may be attributed to the synergistic effect that Nb exerts on palladium and to the bifunctional mechanism [41].

XPS analysis

To obtain information on the oxidation states of Pd and Nb in the near surface region (< 3 nm) of the catalysts, high-resolution Pd 3d and Nb 3d core level XPS spectra were recorded. As displayed in Fig. 8, the deconvoluted Pd 3d spectra

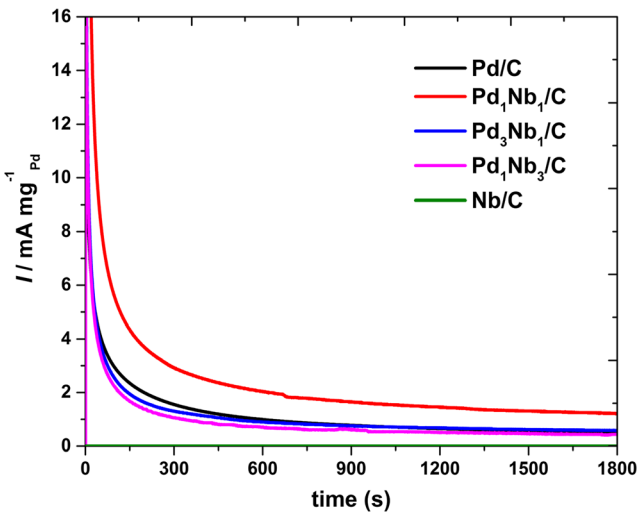

Fig. 7 Chronoamperometry at − 0.40 V of Pd_xNb_y/C electrocatalysts, using 1.0 mol L^{-1} ethanol in 1.0 mol L^{-1} KOH

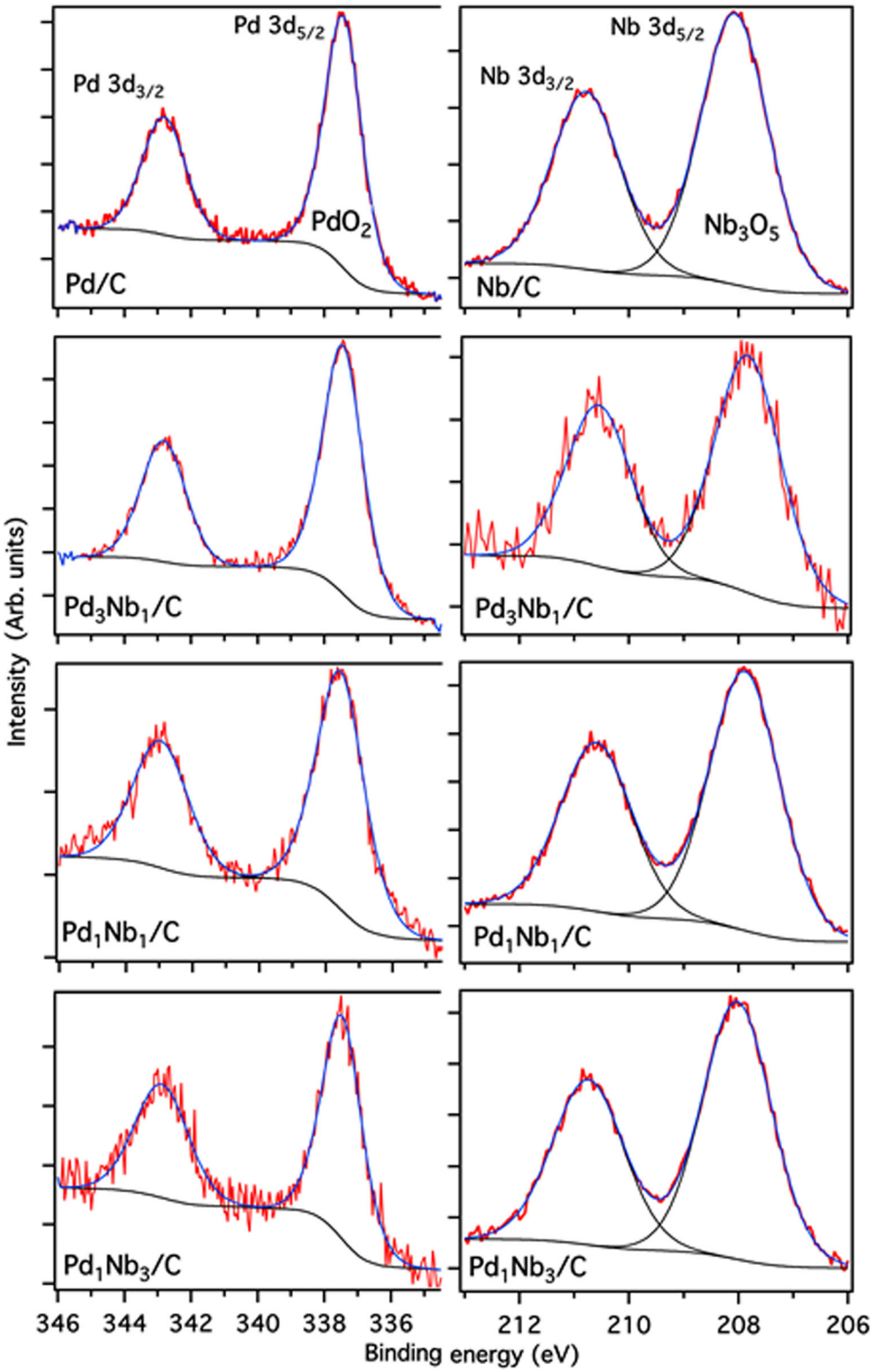

Fig. 8 High-resolution Pd 3d and Nb 3d core-level XPS spectra recorded for Pd_xNb_y electrocatalysts

exhibit a spin–orbit doublet with Pd $3d_{5/2}$ and Pd $3d_{3/2}$ binding energy subpeaks at 337.5 and 342.9 eV, respectively, that are associated with the PdO_2 phase [42]. The binding energies of the Nb $3d_{5/2}$ and Nb $3d_{3/2}$ spin–orbit doublet, centred at 207.8 and 210.6 eV, respectively, are characteristic of the Nb_2O_5 phase [43]. The detected chemical shifts of both spectra support the XRD results, indicating the presence of only pure oxide phases for both elements in the nanoparticle shell. Also, the identified oxidation states agree with the XRD results, although no metallic phase was detected at the low

energy tail of the Pd 3d and Nb 3d spectra. The average particle size of the catalysts (3–10 nm) being larger than the exponentially decaying XPS sampling depth (3Λ~3 nm), $\Lambda \approx 1$ nm being the electron inelastic mean free path of photoelectrons that were ejected from the Pd 3d and Nb 3d orbitals, might explain the absence of a component related to the metallic phase in the nanoparticle core, which was expected at approximately 335 and 202 eV for Pd 3d an Nb 3d, respectively.

Conclusions

Pd_xNb_y/C electrocatalysts were successfully synthesized using the sol–gel method. The addition of Nb to Pd electrocatalysts significantly changed their electrochemical EOR activities in alkaline medium. Among the electrocatalysts that were tested, Pd_1Nb_1/C samples, with a Pd/Nb mass ratio of 1:1, showed superior activity. This electrocatalyst showed 2.2 times higher ECSA, 1.7 times higher CV peak current density and 1.5 times higher CA current density than Pd/C did.

Pd_1Nb_1/C samples also showed the lowest EOR onset potential of the studied electrocatalysts. The promoting effect of Nb can be explained by the bifunctional mechanism in which Nb would adsorb and increase the concentration of OH^- species in proximity to Pd and thus favour the oxidation of intermediates that were adsorbed on the Pd surface. These results demonstrate the possibility of replacing some Pd with Nb in a 50:50 ratio to improve electrochemical activity. Moreover, the addition of Nb in the Pd/C reduces CO_{ads} poisoning of the electrocatalyst. Therefore, Nb is a promising co-catalyst in Pd-based electrocatalysts for electrocatalysis of ethanol in alkaline medium.

References

1. Spinacé E, Neto A, Linardi M (2004) Electro-oxidation of methanol and ethanol using PtRu/C electrocatalysts prepared by spontaneous deposition of platinum on carbon-supported ruthenium nanoparticles. J Power Sources 129:121–126
2. Wendt H, Götz M, Linardi M (2000) Fuel cell technology. Quím Nova 23:538–546
3. Yu H, Zhou D, Zhu H (2014) Synthesis and characterization of Pd-La (OH) 3/C electrocatalyst for direct ethanol fuel cell. J Solid State Electrochem 18(1):125–131
4. Guisbiers G, Khanal S, Ruiz-Zepeda F et al (2014) Cu–Ni nanoalloy: mixed, core–shell or Janus nano-particle? Nano 6:14630–14635
5. Choi YH, Jang YJ, Park H et al (2017) Carbon dioxide Fischer-Tropsch synthesis: a new path to carbon-neutral fuels. Appl Catal B Environ 202:605–610
6. Zhang Y, Zhang H, Zhai Y et al (2007) Investigation of self-humidifying membranes based on sulfonated poly (ether ether ketone) hybrid with sulfated zirconia supported Pt catalyst for fuel cell applications. J Power Sources 2:323–329
7. Assumpção MHMT, da Silva SG, de Souza RFB et al (2014) Direct ammonia fuel cell performance using PtIr/C as anode electrocatalysts. Int J Hydrog Energy 39:5148–5152
8. Nandenha J, De Souza RFB, Assumpção MHMT et al (2013) Preparation of PdAu/C-Sb2O5·SnO2 electrocatalysts by borohydride reduction process for direct formic acid fuel cell. Ionics (Kiel) 19:1207–1213
9. Geraldes AN, Furtunato Da Silva D, Martins Da Silva JC et al (2015) Palladium and palladium-tin supported on multi wall carbon nanotubes or carbon for alkaline direct ethanol fuel cell. J Power Sources 275:189–199
10. Brouzgou A, Podias A, Tsiakaras P (2013) PEMFCs and AEMFCs directly fed with ethanol: a current status comparative review. J Appl Electrochem 43:119–136
11. Pacheco Santos V, Del Colle V, de Lima RB, Tremiliosi-Filho G (2007) In situ FTIR studies of the catalytic oxidation of ethanol on Pt(111) modified by bi-dimensional osmium nanoislands. Electrochim Acta 52:2376–2385
12. Antonin V, Assumpcao M, Silva J, Parreira L (2013) Synthesis and characterization of nanostructured electrocatalysts based on nickel and tin for hydrogen peroxide electrogeneration. Electrochim Acta 109:3431–3450
13. Ziolek M (2003) Niobium-containing catalysts—the state of the art. Catal Today 78:47–64
14. Antolini E, Gonzalez ER (2010) Alkaline direct alcohol fuel cells. J Power Sources 195:3431–3450
15. Yang Z-Z, Liu L, Wang A-J et al (2017) Simple wet-chemical strategy for large-scaled synthesis of snowflake-like PdAu alloy nanostructures as effective electrocatalysts of ethanol and ethylene glycol oxidation. Int J Hydrog Energy 42:2034–2044
16. Liu Q, Xu Y, Wang A, Feng J (2016) A single-step route for large-scale synthesis of core–shell palladium@platinum dendritic nanocrystals/reduced graphene oxide with enhanced electrocatalytic. J Power Sources 302:394–401
17. Wang Q, Lu X, Xin Q, Sun G (2014) Polyol-synthesized Pt2.6Sn1Ru0.4/C as a high-performance anode catalyst for direct ethanol fuel cells. Chinese J Catal 35:1394–1401
18. Neto AO, Dias RR, Tusi MM et al (2007) Electro-oxidation of methanol and ethanol using PtRu/C, PtSn/C and PtSnRu/C electrocatalysts prepared by an alcohol-reduction process. J Power Sources 1:87–91
19. Yi Q, Niu F, Song L et al (2011) Electrochemical activity of novel titanium-supported porous binary Pd-Ru particles for ethanol oxidation in alkaline media. Electroanalysis 23:2232–2240
20. Zhang J, Zhang B, Zhang X (2016) Enhanced catalytic activity of ternary NiCoPd nanocatalyst dispersed on carbon nanotubes toward methanol oxidation reaction in alkaline media. J Solid State Electrochem 21:447–453
21. Lović J, Jović V (2017) Electrodeposited Pd and PdNi coatings as electrodes for the electrochemical oxidation of ethanol in alkaline media. J Solid State Electrochem. https://doi.org/10.1007/s10008-017-3595-2
22. Kamarudin MZF, Kamarudin SK, Masdar MS, Daud WRW (2013) Review: direct ethanol fuel cells. Int J Hydrog Energy 38:9438–9453
23. Suffredini H, Tricoli V, Avaca L, Vatistas N (2004) Sol–gel method to prepare active Pt–RuO 2 coatings on carbon powder for methanol oxidation. Electrochemistry 10:1025–1028
24. Shirley D (1972) High-resolution X-ray photoemission spectrum of the valence bands of gold. Phys Rev B 12:4709
25. Wang Y, Nguyen TS, Liu X, Wang X (2010) Novel palladium–lead (Pd–Pb/C) bimetallic catalysts for electrooxidation of ethanol in alkaline media. J Power Sources 195:2619–2622
26. Ting C, Liu C, Tai C et al (2015) The size effect of titania-supported Pt nanoparticles on the electrocatalytic activity towards methanol

oxidation reaction primarily via the bifunctional mechanism. J Power Sources 280:166–172
27. Wang R, Liao S, Ji S (2008) High performance Pd-based catalysts for oxidation of formic acid. J Power Sources 1:205–208
28. Prabhu Y, Rao K, Kumar V, Kumari B (2014) X-ray analysis by Williamson-Hall and size-strain plot methods of ZnO nanoparticles with fuel variation. World J Nano Sci Eng 4:21
29. Marcelo L (2010) Livros Introdução à Ciência e Tecnologia de Células a Combustível. Artliber, São Paulo
30. Cheng K, Jiang J, Kong S et al (2016) Pd nanoparticles support on rGO-C@ TiC coaxial nanowires as a novel 3D electrode for NaBH 4 electrooxidation. Int J Hydrog Energy 42:2943–2951
31. Qiu X, Dai Y, Tang Y et al (2015) One-pot synthesis of gold–palladium@palladium core–shell nanoflowers as efficient electrocatalyst for ethanol electrooxidation. J Power Sources 278: 430–435
32. Ji Y, Ying Y, Pan Y et al (2016) Palladium networks decorated by cuprous oxide for remarkably enhanced electrocatalytic activity of methanol oxidation reaction with high CO-tolerance. J Power Sources 329:115–122
33. Hong J, Kim Y, Wi D et al (2016) Ultrathin free-standing ternary-alloy nanosheets. Angew Chem 55(8):2753–2758
34. Li G, Xu H, Lu X et al (2015) PdCo nanotube arrays supported on carbon fiber cloth as high-performance flexible electrocatalysts for ethanol oxidation. Angew Chem Int Ed 54(12):3669–3673
35. Wang A, He X, Lu X, Xu H (2015) Palladium–cobalt nanotube arrays supported on carbon fiber cloth as high-performance flexible electrocatalysts for ethanol oxidation. Angew Chem Int Ed 54(12): 3669–3673
36. Cui Q, Chao S, Bai Z et al (2014) Based on a new support for synthesis of highly efficient palladium/hydroxyapatite catalyst for ethanol electrooxidation. Electrochim Acta 132:31–36
37. Zhang K, Xiong Z, Li S et al (2017) Cu 3 P/RGO promoted Pd catalysts for alcohol electro-oxidation. J Alloys Compd 706:89–96
38. Zeinalipour-Yazdi CD, Willock DJ, Thomas L et al (2016) CO adsorption over Pd nanoparticles: a general framework for IR simulations on nanoparticles. Surf Sci 646:210–220
39. Head AR, Karslıoğlu O, Gerber T et al (2017) CO adsorption on Pd(100) studied by multimodal ambient pressure X-ray photoelectron and infrared reflection absorption spectroscopies. Surf Sci 665: 51–55
40. Martin NM, Van den Bossche M, Grönbeck H et al (2014) CO adsorption on clean and oxidized Pd(111). J Phys Chem C 118(2): 1118–1128
41. Geraldes AN, da Silva DF, e Silva LG de A, et al (2015) Binary and ternary palladium based electrocatalysts for alkaline direct glycerol fuel cell. J Power Sources 293:823–830
42. AV. Naumkin, A. Kraut-Vass, S.W. Gaarenstroom CJP NIST X-ray photoelectron spectroscopy (XPS) database, Version 3.5. https://srdata.nist.gov/xps/. Accessed 13 Apr 2017
43. AV. Naumkin, A. Kraut-Vass, S.W. Gaarenstroom CJP NIST X-ray photoelectron spectroscopy (XPS) database, Version 3.5